STRUCTURAL BIOLOGY

Structural basis for the substrate recognition and transport mechanism of the human y$^+$LAT1-4F2hc transporter complex

Lu Dai[1,2]†, Qian Zeng[1,2]†, Ting Zhang[1,2]†, Yuanyuan Zhang[3]†, Yi Shi[3]†, Yaning Li[4]†, Kangtai Xu[1,2], Jing Huang[3]*, Zilong Wang[1,2]*, Qiang Zhou[3]*, Renhong Yan[1,2]*

Heteromeric amino acid transporters (HATs), including y$^+$LAT1-4F2hc complex, are responsible for transporting amino acids across membranes, and mutations in y$^+$LAT1 cause lysinuric protein intolerance (LPI), a hereditary disorder characterized by defective cationic amino acid transport. The relationship between LPI and specific mutations in y$^+$LAT1 has yet to be fully understood. In this study, we characterized the function of y$^+$LAT1-4F2hc complex in mammalian cells and determined the cryo-EM structures of the human y$^+$LAT1-4F2hc complex in two distinct conformations: the apo state in an inward-open conformation and the native substrate-bound state in an outward-open conformation. Structural analysis suggests that Asp^{243} in y$^+$LAT1 plays a crucial role in coordination with sodium ion and substrate selectivity. Molecular dynamic (MD) simulations further revealed the different transport mechanism of cationic amino acids and neutral amino acids. These results provide important insights into the mechanisms of the substrate binding and working cycle of HATs.

INTRODUCTION

Amino acids, as the fundamental building blocks of proteins, are indispensable for sustaining life, participating in multiple critical biological processes within cells (*1*). To maintain cellular balance, amino acid transporters play a pivotal role by facilitating the movement of amino acids across cell membranes (*1*–*3*). Among these, the heteromeric amino acid transporter (HAT) family stands out. Comprising a light and a heavy chain linked by a conserved disulfide bridge, HATs enable the transport of amino acids, polyamines, and drugs across membranes (*4*–*7*).

The light chain of HATs governs substrate specificity and transport activity, while the heavy chain acts as a regulatory subunit essential for proper transporter function (*8*, *9*). 4F2hc (SLC3A2), one of the two known heavy-chain proteins of HATs, is vital for membrane trafficking and transport activity of the light chains (*9*, *10*). Its intracellular N terminus, transmembrane (TM) helix, and extracellular domain are all involved in interactions with the light chains (*9*, *11*, *12*). Beyond its role in amino acid transporters, 4F2hc serves as a cell surface antigen involved in immune responses and as a receptor for certain extracellular matrix proteins (*13*–*15*). Dysregulation and mutations of HATs have been linked to inherited or metabolic disorders such as cystinuria, lysinuric protein intolerance (LPI), and multiple cancers (*16*–*19*).

[1]School of Medicine, Southern University of Science and Technology, Shenzhen, Guangdong Province, China. [2]Key University Laboratory of Metabolism and Health of Guangdong, Institute for Biological Electron Microscopy, Southern University of Science and Technology, Shenzhen, Guangdong Province, China. [3]Research Center for Industries of the Future, Zhejiang Key Laboratory of Structural Biology, School of Life Sciences, Westlake University, Institute of Biology, Westlake Institute for Advanced Study, Westlake Laboratory of Life Sciences and Biomedicine, Hangzhou, Zhejiang Province, China. [4]Beijing Advanced Innovation Center for Structural Biology, Tsinghua-Peking Joint Center for Life Sciences, School of Life Sciences, Tsinghua University, Beijing 100084, China.
*Corresponding author. Email: huangjing@westlake.edu.cn (J.H.); wangzl6@sustech.edu.cn (Z.W.); zhouqiang@westlake.edu.cn (Q.Zh.); yanrh@sustech.edu.cn (R.Y.)
†These authors contributed equally to this work.

The y$^+$LAT1-4F2hc complex is a prototypical member of HATs, facilitating sodium-dependent influx transport of neutral amino acids and sodium-independent influx of dibasic amino acids in an electroneutral exchanging manner studied by the *Xenopus oocyte* system (*17*, *20*, *21*). Specifically, y$^+$LAT1 is prominently expressed in the basolateral membranes of epithelial cells in both the kidney and intestine. Mutations occurring in the gene encoding y$^+$LAT1 are responsible for LPI, a rare metabolic disorder characterized by defective transport of cationic amino acids, particularly lysine, ornithine, and arginine, at the basolateral membranes of intestinal and renal tubular cells (*22*). Predominantly observed in populations from Finland, Japan, Italy, and North Africa, LPI manifests with a spectrum of symptoms including failure to thrive, poor appetite, growth retardation, hepatosplenomegaly, and substantial osteoporosis (*23*–*25*). While specific treatment regimens can help manage LPI, a definitive cure has yet to be discovered (*25*).

Despite the inward-facing and outward-facing occluded cryo–electron microscopy (cryo-EM) structures of the human LAT1-4F2hc complex were determined (*9*, *26*–*28*), in addition to which the available structural information related with HATs includes the crystal structures of bacterial homologs (*29*–*33*), and the varied resolution EM structures of the LAT2-4F2hc, xCT-4F2hc, and Asc-1-4F2hc complex (*10*–*12*, *34*–*39*), the precise transport mechanism of the y$^+$LAT1-4F2hc complex and its correlation with LPI pathogenesis remain elusive. Our study unveils the outward-open cryo-EM structures of the human y$^+$LAT1-4F2hc complex, bound with native substrates L-leucine (Leu), L-lysine (Lys), and L-arginine (Arg), respectively, in an outward-facing conformation. These elucidated structures provide invaluable insights into the intricate mechanisms underlying substrate recognition and transport, thus contributing notably to our understanding of LPI and paving the way for targeted therapeutic interventions.

RESULTS

Structural determination of y$^+$LAT1-4F2hc complex with different substrates

While the function of the y$^+$LAT1-4F2hc complex has been extensively studied using the *Xenopus oocyte* system, its workings within

mammalian cells are less well understood. To investigate its transport properties, we initially characterized the function of the y^+LAT1-4F2hc complex by measuring the currents associated with sodium-Leu cotransport in human embryonic kidney (HEK) 293T cells coexpressing y^+LAT1 and 4F2hc. The results indicated that the y^+LAT1-4F2hc complex efficiently transports Leu with sodium ions and exhibits dose-dependent electrogenic activity (fig. S1, A and B). In addition, microscale thermophoresis (MST) affinity assays revealed comparable binding affinities of the complex for Leu, Lys, and Arg (fig. S1, C to F).

To further explore the impact of sodium ions on the transport of neutral and cationic amino acids, we substituted the sodium chloride buffer with choline chloride (ChoCl) buffer in the cell-based transport assay. Our findings reveal that in the absence of sodium ions, the transport of Leu is nearly undetectable, whereas the transport of Lys and Arg was significantly enhanced, highlighting distinct transport mechanisms for these amino acids (Fig. 1, A and B).

To deepen our understanding of its working mechanism, we determined the cryo-EM structures of the human y^+LAT1-4F2hc complex in both the apo state and bound with native substrates (Leu, Lys, and Arg) at resolutions of 3.7, 3.0, 3.3, and 2.9 Å, respectively (Fig. 1C and fig. S2, A to C). For detailed procedures regarding recombinant cloning, protein overexpression, purification, and structural determination, please refer to Materials and Methods (figs. S3 to S5 and table S1). The overall architecture of the y^+LAT1-4F2hc complex is closely similar to that of the LAT1-4F2hc complex with the 0.822 Å root mean square deviation through 822 amino acids (Fig. 1C and fig. S2D).

In the case of Arg-bound structure, y^+LAT1 comprises 12 TM segments organized into a classical LeuT fold. TM1 to TM5 are linked to TM6 to TM10 through a pseudo twofold symmetry axis parallel to the membrane. TM1, TM2, TM6, and TM7 constitute the helix bundle domain or core domain, while TM3, TM4, TM8, and TM9 form the hash domain. TM1 and TM6 harbor unwound regions at their center, creating a substrate binding site. TM11 and TM12 are oriented antiparallel to TM9 and TM10, followed by a lateral helix at the C-terminal end. 4F2hc extensively interacts with y^+LAT1 at the extracellular side, the TM region, and the intracellular side (Fig. 1C and figs. S2 and S6), resembling the structure of the LAT1-4F2hc complex, another representative member of HAT (*9*). However, the extracellular domain of 4F2hc exhibits greater flexibility in apo state, as well as in Leu-bound or Lys-bound y^+LAT1 compared to Arg-bound y^+LAT1 (Fig. 1C and fig. S2, A to C).

In the extracellular region, additional hydrogen bonds are established between Arg^{288} of y^+LAT1 and Ser^{302} of 4F2hc, enhancing the binding between the 4F2hc and y^+LAT1 when compared with the outward-facing occluded conformation of LAT1 (fig. S7, A and B). Similarly, in the inward-open LAT1 structure, Arg^{535} of 4F2hc in Arg-bound y^+LAT1 partakes in the interaction with the light chain (fig. S7B). The apo structure of the y^+LAT1-4F2hc complex closely resembles the LAT1-4F2hc structure bound to BCH, adopting an inward-open conformation with a slight shift of TM1a and TM6b (fig. S8A).

Substrate binding patterns of y^+LAT1

The substrates Leu, Lys, and Arg of y^+LAT1 are all bound to the unwound regions of TM1 and TM6, with their carboxyl and amino groups hydrogen bonded to the main chain atoms of the transporter (Fig. 2). The side chain of the gating residue Phe^{237}, corresponding to Phe^{252} in LAT1, rotates away from the substrate binding site, resulting in an open conformation and a spacious extracellular vestibule that encompasses a chamber beneath the bound substrate (fig. S8B).

Specifically, the α-carboxylate group of Leu forms three hydrogen bonds with the oxygen atoms of Ile^{51} and the nitrogen atom in Ser^{53} and Gly^{54} in TM1, and the α-amino group of Leu forms hydrogen bonds with the oxygen atoms of Met^{50} and Ile^{51} in TM1, Tyr^{274} in TM7, and Ser^{238} in TM6 (Fig. 2C). The α-carboxylate group of Arg forms several hydrogen bonds with the nitrogen atoms in the main chain of Gly^{52}, Ser^{53}, and Gly^{54}, while the α-amino group of Arg forms hydrogen bonds with the oxygen atoms of Ser^{240} and Ser^{238} in TM6, Tyr^{274} in TM7, and Met^{50} in TM1. The guanidine group of Arg is stabilized by the nitrogen atom of Asn^{49} in TM1 and the oxygen atoms of Ser^{240} in TM6 (Fig. 2B). Similarly, the main chain of Lys is close to that of Arg, while the nonpolar segment of the Lys side chain engages with Gly^{241} in TM6 through hydrophobic interactions. This interaction prompts a shift in the Lys closer to TM6 compared to the Arg-bound structure (Fig. 2D). Notably, since Leu substrate has a relatively short tail and lacks polarity, its side chain mainly interacts with the TM1 via hydrophobic interactions and does not engage in interactions with TM6, while the tail of Arg and Lys engage the interactions with TM1 and TM6, exhibiting a different substrate selectivity mechanism (Fig. 2E).

A putative sodium ion binding site in y^+LAT1

In the region of the cryo-EM map with y^+LAT1 bound with Leu, additional density above background levels may be indicative of a sodium ion, consistent with the presence of 150 mM NaCl in the sample (Fig. 3A). Oxygen atoms from Asp^{243}, Ser^{240}, and Tyr^{389} form a pocket well-positioned to coordinate sodium ion at the center. The average distance in coordination with the sodium ion is 2.7Å. Notably, the side chain of Trp^{242} interacts with the sodium ion via cation-pi interactions (Fig. 3A), potentially contributing to stabilizing Leu in the pocket. Notably, the corresponding ion density is invisible in the Lys-bound structure despite the existence of sodium ion (fig. S9A). Because of the average length of possible formed interaction with the extra density that is above 3.4 Å in the Arg-bound structure, it could not support the building of a sodium ion. We speculated that there is a water molecule rather than sodium ion in that position (fig. S9B).

When comparing the structures of y^+LAT1 bound to three different substrates, it is observed that in the Leu-bound y^+LAT1 structure, Asp^{243} and Tyr^{389} coordinate with sodium ion. Conversely, in the Lys-bound and Arg-bound y^+LAT1 structure, Asp^{243} and Tyr^{389} can engage in hydrogen bond interactions. This special binding pattern might imply the different transport mechanism of y^+LAT1 with neutral amino acids like Leu and cationic amino acids like Arg and Lys (fig. S9, A and B).

Sequence alignment of the HAT family (fig. S10) reveals that they all share the conserved residues as y^+LAT1 at these sites: Phe^{237}, Trp^{242A}, and Tyr^{274}. By combining the key residues in the pocket across the three substrate-bound structural conformations and the residues responsible for the localization of sodium ion, we identified seven potentially critical residues of y^+LAT1 and set up mutations for functional studies: S238A, S240A, W242A, D243A, D243N, Y274A, and Y389A. All mutants, compared to wild-type (WT) y^+LAT1, showed a compromised transport activity but with an equal level of expression and colocation of the plasma membrane,

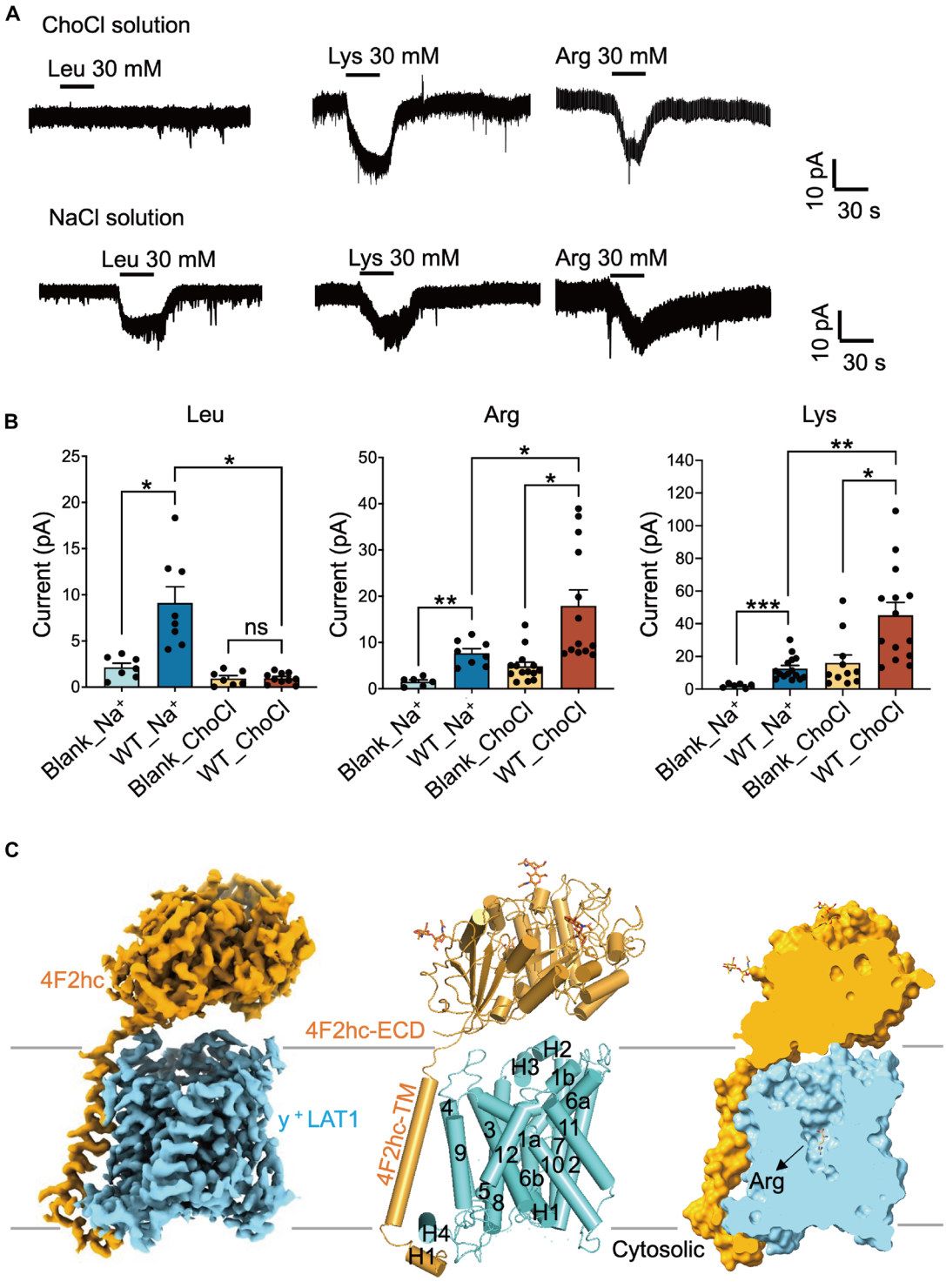

Fig. 1. Overall structures of y$^+$LAT1-4F2hc complex. (**A** and **B**) The absence of sodium ions in extracellular solution hampers the transport of Leu and enhances the transport of Lys and Arg. *P < 0.05, **P < 0.01, and ***P < 0.001, one-way analysis of variance (ANOVA) followed by Tukey's test, data are presented as mean ± SEM. (**C**) Cartoon structure of the y$^+$LAT1-4F2hc Arg-bound (blue) and y$^+$LAT1 adopts an outward-open conformation with Arg in the center of the substrate binding pocket. ns, not significant.

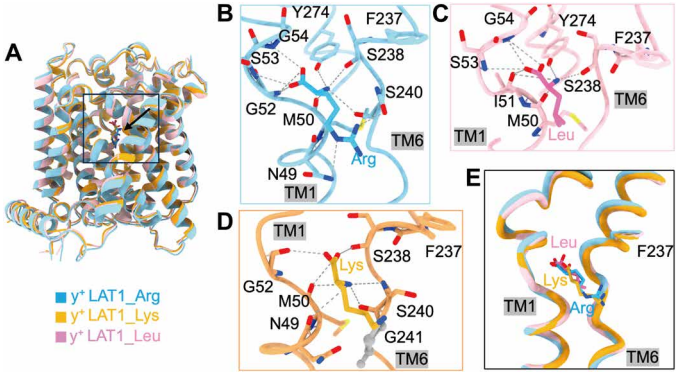

Fig. 2. Three-substrate binding analysis. (**A**) The overall structure of y$^+$LAT1 bound with three different substrates. The direction indicated by the black arrow in the box is the substrate binding site. (**B** to **D**) The interaction networks of Arg (blue), Leu (pink), and Lys (orange) with y$^+$LAT1 are shown. (**E**) Structural comparison of the substrate binding sites of y$^+$LAT1 with Arg, Leu, and Lys. Arg, Leu, and Lys are colored blue, pink, and orange, respectively. The gray dashed lines represent hydrogen bonds, and the gray amino acids are involved in the hydrophobic interactions.

suggesting an important role in substrate coordination and transport (Fig. 3B and fig. S11).

To further elucidate the roles of the Trp^{242} and Asp^{243}, which are implicated in interactions with the sodium ion (Fig. 3A), we performed MST and whole-cell patch-clamp recordings. The results showed that the D243A mutation significantly diminished the binding affinity for Leu, while the W242A mutation had a comparatively minor impact (fig. S1D). This disparity likely stems from the stronger interaction between the side chain of Asp^{243} and the sodium ion (Fig. 3A). Both mutations are critical for maintaining substrate binding stability, which closely aligns with their impact on transport activity fig. S3B). In the case of Lys, both W242A and D243A mutations caused a significant decrease in binding affinity and substantially impaired transport activity, despite the absence of direct interactions with Lys in the solved structure (Fig. 3C and fig. S1E). This suggests that the interactions involving Trp^{242} and Asp^{243} are essential for stabilizing Lys during key stages of the transport process. In contrast, these mutations did not significantly affect Arg binding affinity and transport activity (Fig. 3D and fig. S1F), implying that Arg binding is less dependent on these particular residues. Together, these findings imply that the y$^+$LAT1-4F2hc complex may use distinct mechanisms for the transport of neutral versus dibasic amino acids.

Molecular dynamic simulation for the sodium binding

To further evaluate the role of sodium ion during substrate transport, we performed a series of molecular dynamic (MD) simulations with CHARMM36m (C36m) force field (Fig. 4, fig. S12, and movie S1). We observe that the α-carboxylate group of the substrate can bind to the pocket through polar interactions with Ser^{53} and Gly^{54} in TM1 for hundreds of nanoseconds, despite the dissociation event can be observed for all three substrates. The α-amino group of three substrates can form hydrogen bond with oxygen atoms of Ser^{240} and Ser^{238}. Facilitated by additional contacts, the Lys and Arg substrates are prone to interact with Ser^{240}. Notably, besides Asn^{49}, a salt bridge between the guanidino group of the substrate Arg and Glu^{128} can be formed, stabilizing the Arg pose of pointing the α-amino group of

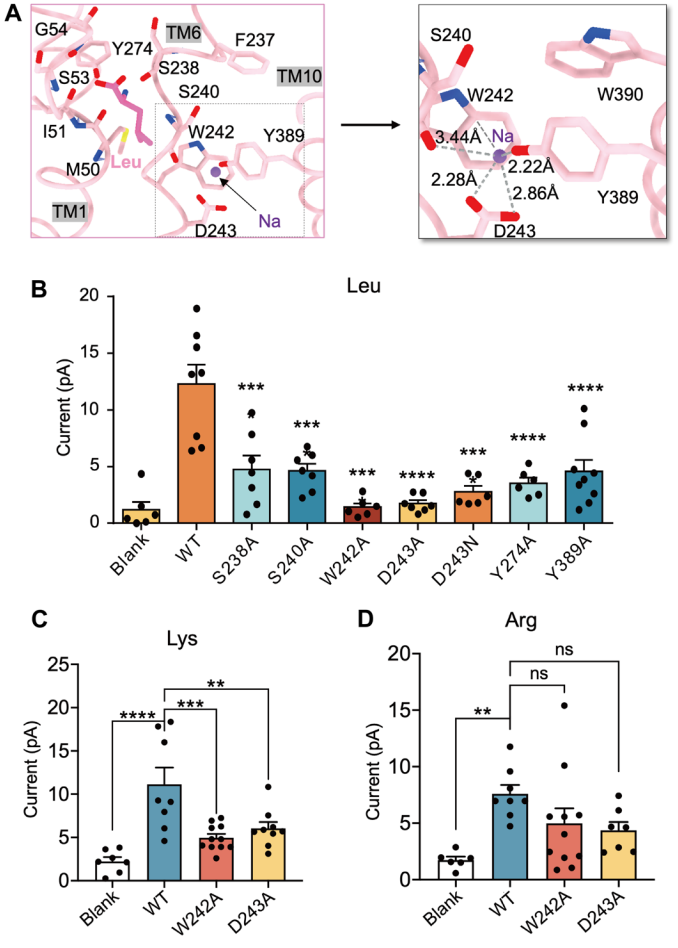

Fig. 3. Na$^+$ binding site in the y$^+$LAT1-4F2hc Leu-bound structure. (**A**) The interaction interface of the Na$^+$ binding site and the polar interactions are shown as gray dashes. Leu is displayed as bright pink, and the sodium ion is displayed as purple. (**B**) Key residue mutations inhibit the transport activity of y$^+$LAT1, currents induced by 30 mM Leu. ****$P < 0.0001$, compared with WT-y$^+$LAT1 and calculated by one-way ANOVA followed by Tukey's test. Data present mean ± SEM. (**C**) W242A and D243A mutations inhibit the transport activity of y$^+$LAT1. Currents were induced by 30 mM Lys perfusion. ***$P < 0.001$ and **$P < 0.01$ compared with WT-y$^+$LAT1, calculated by one-way ANOVA followed by Tukey's test. (**D**) W242A and D243A mutations have no effect on the transport activity of y$^+$LAT1. Currents were induced by 30 mM Arg perfusion; not significant compared with WT-y$^+$LAT1, calculated by one-way ANOVA followed by Tukey's test. Data are presented as mean ± SEM.

Arg toward Ser^{240} in the Arg-bound structure. In the Lys-bound structure, the ε-ammonium group can form a hydrogen bond with the hydroxyl group Ser^{131} and Ser^{240}, and the additional contacts with Ser^{240} can provide stronger interactions. This result is consistent with our cryo-EM observations.

First, all the sodium unbinding events are observed in our simulations for the identified sodium binding pocket. We then speculated that cation-π interaction between sodium ion and the indole ring of the side chain in Trp^{242} might contribute to stabilizing sodium binding into the pocket formed by Asp^{243}, Trp^{242}, Ser^{240}, and Tyr^{389}. It is well-known that additive protein force fields such as C36m underestimate cation-π interaction (*40*), so we performed MD simulations with an ad hoc fix to C36m with Non-Bonded FIX (NBFIX) parameters fitting based on high level quantum mechanics calculations

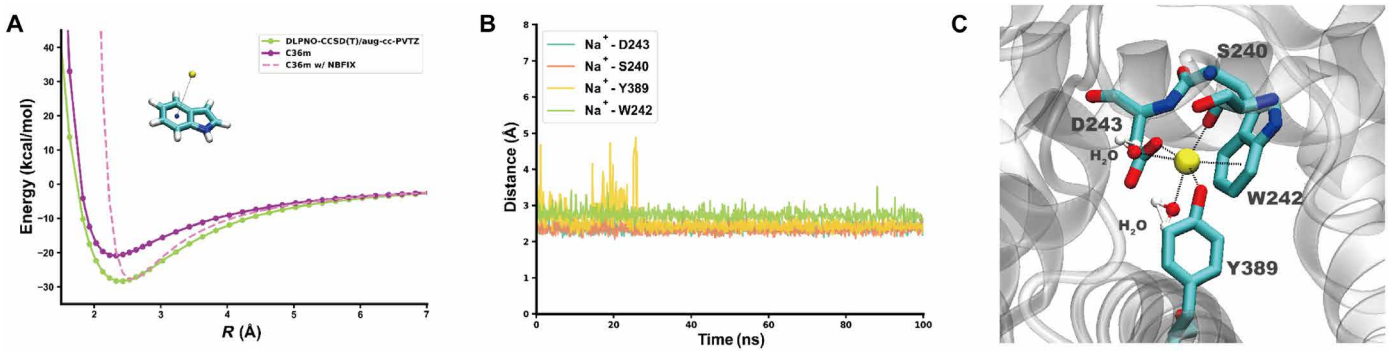

Fig. 4. MD simulations for the Na^+ binding site. (**A**) The interaction energy scan for a Na^+ and indole was obtained using DLPNO-CCSD(T) methods with aug-cc-pVTZ basis set (green line) in comparison with that using C36m force field (purple line) by varying the distance at the direction perpendicular to the indole six-membered ring. The dashed pink line represents the NBFIX modification to C36m that restores the QM cation-π interactions between the sodium ion and indole. (**B**) The distance between Na^+ and the minimum carboxyl oxygen of Asp^{243}, the hydroxyl oxygen of Tyr^{389}, backbone oxygen of Ser^{240}, and the six-membered ring center of Trp^{242} during the simulation with NBFIX modification. (**C**) Snapshot of the simulation with NBFIX modification for the sodium binding pocket. The two water molecules coordinated with Na^+ were also highlighted.

(Fig. 4A). Simulations based on such a modified force field can result in a stable binding mode of Na^+ under a timescale of more than 100 ns. In this conformation, the Trp^{242}, Asp^{243}, Tyr^{389}, and oxygen of Ser^{240} backbone are well coordinated with sodium ion (Fig. 4, B and C). In addition, two water molecules were involved in stabilizing the sodium ion (Fig. 4C). These results also suggest a reason why sodium cannot be observed in Lys and Arg binding structures due to the larger impact on Ser^{240}.

Conformational changes induced by substrate binding

When aligning the three substrate-bound structures with y^+LAT1, we observed that the binding positions of the y^+LAT1-4F2hc complex bound to Lys and Leu are highly similar, with TM1 and TM6 superimposing well, despite their differing charging properties and structures (Fig. 2E).

We also compared the outward-open conformation of y^+LAT1 with the inward-open conformation of y^+LAT1 and the outward-occluded in LAT1 3,5-diiodo-L-tyrosine–bound structure (*27*), respectively, and revealed the movement of TM1, TM6, and TM10 (Fig. 5, A and B). The TM1 and TM6 are notably rotated to open the extracellular tubule and subsequently the open of Phe^{237}, leading to a more outward-open state (Fig. 5, A and B). This conformational change represents a unique feature within the HAT family and potentially indicating the next step in the transport cycle of y^+LAT1. The entire transport process of the HATs can be inferred from the states of the conserved gating residue, including Phe^{252} in the inward-open conformation of LAT1, Phe^{252} in the outward-occluded conformation of LAT1, and Phe^{237} in the outward-open conformation of y^+LAT1 (fig. S8B).

Mapping of LPI-related mutations

The mutations in y^+LAT1 are associated with LPI, yet their specific effects on the transport activity of the complex remain elusive. In this study, we used the structures presented herein to map LPI-related mutations, which are dispersed throughout the entire sequence, onto the three-dimensional (3D) structure. These mutations were classified into three categories (Fig. 6) (*41*, *42*). Class I mutations, including M50K, S53L, G54V, and S238F, are situated along the putative transport path. Class II mutations, encompassing T188I, K191E,

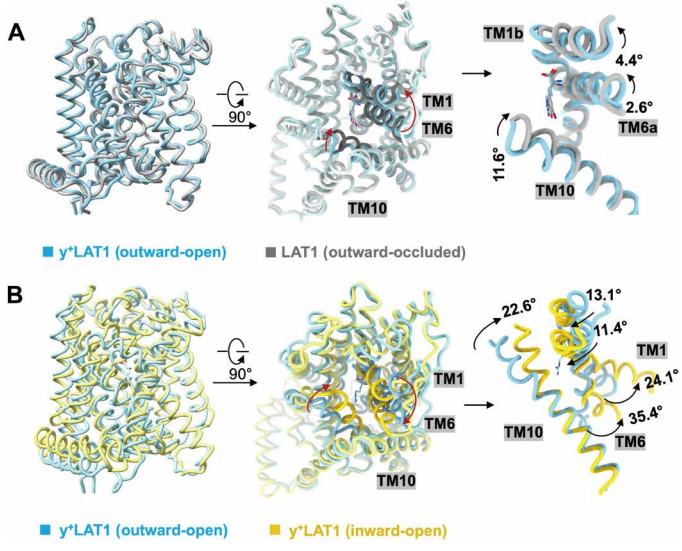

Fig. 5. The conformational change of y^+LAT1. (**A** and **B**) Structural comparison among the y^+LAT1-4F2hc bound with Arg (blue), the outward-occluded structure of LAT1 bound with 3,5-diiodo-L-tyrosine (gray), and the inward-open structure of y^+LAT1 apo (yellow). The movements of TM1 and TM6 are shown in the middle and right, respectively.

E251D, R333M, L334R, G338D, N365Y, and S386R, may influence transport activity by altering the local environment at these sites. Notably, Glu^{251} and Arg^{333} form a salt bridge in the WT protein. In addition, Lys^{191} of y+LAT1, corresponding to Lys^{154} in BasC (*29*), occupies a position equivalent to Na2. Class III mutations involve substitutions to proline (L124P, A140P, L261P, and S489P), which could affect the secondary structure and/or conformational changes during the transporter's working cycle.

DISCUSSION

In this study, we systematically describe the transport of various amino acids by y^+LAT1-4F2hc complex, providing further insights into the transport mechanism of HAT family members. While much of

the fundamental transport activity was previously established (*20*), our research highlights the use of HEK-293T cells for patch-clamp studies, which reveals more detailed aspects of transport dynamics.

Among the light-chain proteins of HAT, y^+LAT1 and y^+LAT2 are unique in mediating both sodium-dependent influx of neutral amino acids and sodium-independent influx of cationic amino acids. In the *Xenopus oocyte* system, the efflux of cationic amino acids like Arg occurs in exchange with an uptake buffer containing sodium or with Leu or Arg alone, but no Leu efflux is mediated by the y^+LAT1-4F2hc heterodimer. This transport property is considered electroneutral (*17*, *20*, *21*). In contrast, our study uses whole-cell patch-clamp recordings in mammalian cells to characterize the electrogenic transport of sodium-dependent leucine and sodium-independent lysine by the y^+LAT1-4F2hc complex. Mutations in key residues significantly reduce the transport activity of the y^+LAT1-4F2hc complex, confirming this transport property. We speculate that the electrogenic nature of the complex results from the excessive influx of sodium ions, lysine, or arginine during the transport cycle.

In addition, the study of point mutations Trp^{242} and Asp^{243} provides evidence that the transporter operates through distinct transport modes for cationic and neutral amino acids, depending on sodium dependency. Within the cationic amino acids, Lys and Arg exhibit different binding affinities with W242A and D243A mutations and transport activities, highlighting a unique transport mode for each substrate.

Sequence alignment and structural analysis of these light-chain proteins revealed a negatively charged residue at position Asp^{243}, which may coordinate a sodium ion in the structure of Leu-bound y^+LAT1-4F2hc in an average distance of 2.7Å (Fig. 3A and fig. S10). We also compared the Leu-bound structure with the apo structure, and the outward-facing occluded conformation of LAT1 (fig. S13A). When compared with these structures, the side chain of Tyr^{389} shows an obvious shift toward TM6 in the apo structure, which could notably decrease the average distance of sodium ion coordination, implying more stable binding of the sodium ion in this conformation (fig. S13B).

Given that LAT1, LAT2, Asc-1, and $b^{0,+}$AT (*43*, *44*) mediate the influx of the neutral amino acids, while xCT catalyzes the influx of negative charged cystine, and all of these transporters work in a sodium-independent manner, we speculated the Asp^{243} of y^+LAT1 plays an important role for the selectivity of neutral amino acids and cationic amino acids. The corresponding residue of Asp^{243} in y^+LAT1 is corresponding to Asn^{258} in LAT1, which was shown to be critical for the transport activity of LAT1. Upon y^+LAT1 transports a neutral amino acid into the cell, Asp^{243} is neutralized by a sodium ion. When the transporter undergoes a conformational change from the outward-facing state to the inward-facing state, the neutral substrate and sodium ion will be released into the cytosol, and the negative charge of Asp^{243} might facilitate the binding of cationic amino acids in the cytoplasm to the y^+LAT1-4F2hc transporter complex.

The structures of outward-open conformation of the y^+LAT1-4F2hc complex greatly expand the mechanistic understanding of human HATs. Since the highly conserved sequence identity, we speculate that y^+LAT1 and LAT1 probably share a conserved structure and a transport mechanism (fig. S10). Structural comparison between the present y^+LAT1-4F2hc complex and the LAT1-4F2hc complex show that the interfaces between the light-chain transporter and 4F2hc are conserved in both the outward-facing and the inward-facing conformations, confirming the previous model that 4F2hc might appear to stabilize the scaffolding domain of light chain during an alternating-access cycle. The rotation of the core domain leads to the close of the intracellular vestibule and opening the extracellular vestibule, which is similar to the working mechanisms investigated in the bacterial homologs (*32*, *45*, *46*). The TMs 10, 11, and 12 also undergo rotation alongside with the core domain during the conformation cycle of the transporter, resulting in a substantial movement of the IL_{10-11} loop, locking of which may inhibit the transport activity of the transporter (*47*).

On the basis of this structural analysis, we propose a selective working model for y^+LAT1 (Fig. 7). y^+LAT1 loads extracellular substrates (possible neutral amino acids with sodium ion or cationic amino acids alone), and then TM1b and TM6a rotate to close the outward gate. During the transition from the outward-open conformation to the outward-occluded conformation, the rotation of TM1b and TM6a triggers the close of the gating residue Phe^{237} to the

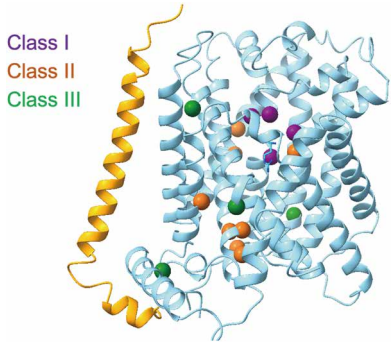

Fig. 6. LPI-related mutations mapping in the y^+LAT1. LPI-related mutations mapping in the complex, which can be classified into classes I, II, and III that are colored in purple, orange, and green, respectively.

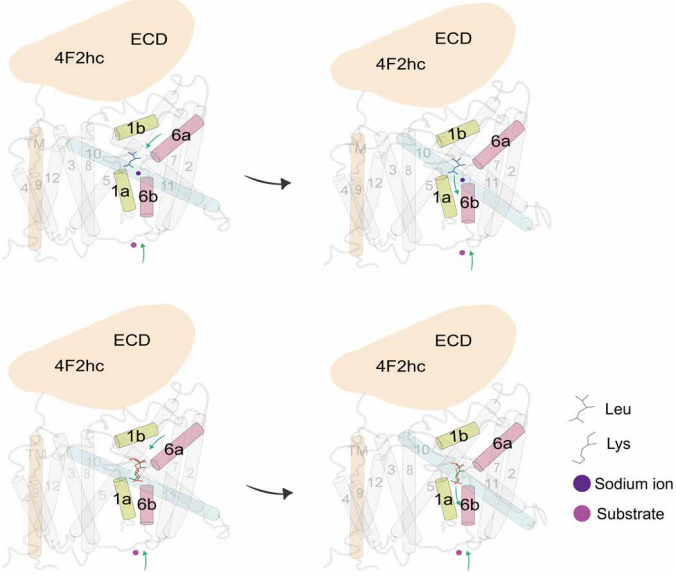

Fig. 7. Putative working model for the y^+LAT1-4F2hc complex. The model shows a transport mechanism of y^+LAT1. y^+LAT1 loads extracellular substrates, and then TM1b and TM6a rotate to close the outward gate. During the transition from the outward-open conformation to the outward-occluded conformation, the rotation of TM1b and TM6a triggers the close of the gating residue Phe^{237} to the occluded configuration. At the same time, the TM10 are also involved in an obvious shift. ECD, extracellular domain of 4F2hc.

occluded configuration. At the same time, the TM10 is also involved in an obvious shift to trigger the transfer of substrate. In summary, the high-resolution structures of the y^+LAT1-4F2hc complex in outward-open conformation reported in this work represent a major step toward a detailed mechanistic understanding of human HATs.

MATERIALS AND METHODS

Protein expression and purification

The full-length human cDNA of y^+LAT1 (accession number: NM_001126105.3) was subcloned into pCAG with N-terminal FLAG tag and 4F2hc (isoform b, accession number: NM 001012662.2) into pCAG with N-terminal 10xHis tag from a cDNA library generated from HEK-293T cells. The mutations were generated by a standard two-step polymerase chain reaction. To ensure the utmost quality, all maxim-plasmids used for cell transfection underwent preparation using the GoldHi Endo Free Plasmid Maxi Kit Beijing Com Win Biotech Co., Ltd. (CWBIO). Plasmid quality was assessed using the Trans2K Plus DNA Marker (TransGen Biotech).

The recombinant protein was produced through overexpression in HEK-293F mammalian cells at 37°C within a Multitron-Pro shaker (Infors), maintaining a consistent speed of 130 rpm and an environment of 5% CO_2. To achieve coexpression of y^+LAT1 and its mutations and 4F2hc, cells underwent transient transfection using the plasmids and polyethyleneimines (PEIs) (Yeasen, 40816ES03). This transfection occurred when the cell density reached approximately 2.0×10^6/ml. For the transfection of 1 liter of cell culture, around 0.75 mg of y^+LAT1 plasmids and 0.75 mg of 4F2hc plasmids were premixed with 3 mg of PEIs in 50 ml of fresh medium, allowing them to interact for 15 min before being introduced into the cell culture. The transfected cells were cultivated for a duration of 48 to 60 hours before the harvesting process commenced. After the completion of 60 hours of transfection, cells were collected by subjecting them to centrifugation at 3500*g* for a duration of 15 min. Subsequently, they were resuspended in a buffer comprising 25 mM Hepes (pH 7.5), 150 mM NaCl, and a combination of three protease inhibitors: aprotinin (1.3 μg/ml; Macklin, A6353), pepstatin (0.7 μg/ml; Macklin, P6117), and leupeptin (5 μg/ml; Macklin, L812486).

The extraction and purification of the y^+LAT1-4F2hc complex were carried out following established methods. First, the membrane fraction was solubilized at 4°C for 2 hours using 1% (w/v) Lauryl Maltose Neopentyl Glycol (LMNG) (Anatrace, NG310) supplemented with 0.1% (w/v) cholesteryl hemisuccinate tris salt (Anatrace, CH210). Subsequently, cell debris was removed via centrifugation at 15,000*g* for 45 min. The resulting supernatant was then applied to anti-FLAG M2 affinity resin (GenScript, L00432). Following this step, the resin was thoroughly rinsed with a wash buffer that consisted of 25 mM Hepes (pH 7.5), 150 mM NaCl, and 0.02% (w/v) glycodiosgenin (GDN) (Anatrace, GDN101). The protein of interest was subsequently eluted using the wash buffer supplemented with FLAG peptide (0.2 mg/ml). Then, elution of anti-FLAG M2 affinity resin was further purified with Nickel-Nitrilotriacetic Acid (Ni-NTA) affinity resin (QIAGEN, 30230). Wash buffer and elution buffer of nickel resin were the wash buffer mentioned above plus 10 and 300 mM imidazole, respectively. Then, the protein complex was subjected to size exclusion chromatography (Superose 6 Increase 10/300 GL, GE Healthcare) in buffer containing 25 mM Hepes (pH 7.5), 150 mM NaCl, and 0.02% GDN. The peak fractions were collected and concentrated for EM analysis.

Cryo-EM sample preparation and data acquisition

The protein of y^+LAT1-4F2hc complex was incubated with 2 mM Lys, 2mM Leu, or 10 mM Arg. Protein mixtures were concentrated to 10 mg/ml, and aliquots (3.5 μl) of the mixture were placed on glow-discharged holey carbon grids (Quantifoil Au R1.2/1.3), which were blotted for 3.0 or 3.5 s and flash-frozen in liquid ethane cooled by liquid nitrogen with Vitrobot (Mark IV, Thermo Fisher Scientific). The cryo-grids were transferred to a Titan Krios operating at 300 kV equipped with a Gatan K3 Summit detector and a Gatan Imaging Filter (GIF) Quantum energy filter. Movie stacks were automatically collected using AutoEMation (*48*), with a slit width of 20 eV on the energy filter and a defocus range from −1.2 to −2.2 μm in super-resolution mode at a nominal magnification of ×81,000. Each stack was exposed for 2.56 s with an exposure time of 0.08 s per frame, resulting in a total of 32 frames per stack. The total dose rate was approximately 50 $e^-/Å^2$ for each stack. The stacks were motion-corrected with MotionCor2 (*49*) and binned twofold, resulting in a pixel size of 1.087, 0.855, or 0.827 Å/pixel. Meanwhile, dose weighting was performed (*50*). The defocus values were estimated with Gctf (*51*).

Data processing

The particles of y^+LAT1-4F2hc bound with Arg were automatically picked from manually selected micrographs using Relion 3.0 (*52*–*55*). After 2D classification, good particles were selected and subjected to a global angular searching 3D classification using the cryo-EM map of the LAT1-4F2hc complex as the initial model with only one class. For each of the last several iterations of the global angular searching 3D classification, a local angular searching 3D classification was performed, during which the particles were classified into four classes. Nonredundant good particles were selected from the local angular searching 3D classification. Then, these selected particles were subjected to multireference 3D classification, local defocus correction, 3D autorefinement, and postprocessing. To further improve the map quality in the TM region, focused 3D classification and autorefinement were performed by applying appropriate mask on the TM region. The 2D classification, 3D classification, and 3D autorefinement were performed with Relion 3.0 The resolution was estimated with the gold-standard Fourier shell correlation 0.143 criterion (*56*) with high-resolution noise substitution (*57*). The y^+LAT1-4F2hc bound with Leu and Lys and in apo state of cryo-EM structures was solved cryoSPARC (*58*). Patch-based contrast transfer function (CTF) estimation was used to estimate the CTF correction parameters of micrographs in cryoSPARC. Particles were automatically picked using Template picker. Several rounds of 2D classification were performed, and the selected particles from 2D classification were subject to several cycles of heterogeneous refinement with C1 symmetry. Particles from the best class were subjected to nonuniform refinement and local CTF refinement. The resolution was estimated with the gold-standard Fourier shell correlation 0.143 criterion (*56*) with high-resolution noise substitution (*57*). Refer to Materials and Methods, figs. S3 to S5, and table S1 for details of data collection and processing.

Model building and structure refinement

The model building was accomplished with Phenix (*59*) and Coot (*60*). The AlphaFold predict atomic model of the y^+LAT1-4F2hc was used for the initial model of y^+LAT1-4F2hc apo state, y^+LAT1-4F2hc bound with Arg, y^+LAT1-4F2hc bound with Lys, and y^+LAT1-4F2hc bound with Leu and fitted into focused refined maps of substrate binding part

using MDFF (MD flexible fitting) (*61*). Except for the Arg-bound structure, where the 4F2hc density was well-resolved, the other structures exhibited weak 4F2hc density, preventing model building. Certain regions, including the cytoplasmic N terminus and C terminus among these structures, were not resolved. These regions likely exhibit flexibility, which could account for their lack of resolution in our structural data. Furthermore, these unresolved loop regions are not involved in substrate recognition or transport, so their absence does not affect the functional analysis. Each residue was manually checked with Coot with the chemical properties taken into consideration during model building. Statistics associated with data collection, 3D reconstruction, and model building are summarized in table S1.

MST assay

MST experiments were conducted using a Monolith NT.115 (NanoTemper Technologies, Munich, Germany). Green fluorescent protein (GFP)–tagged y^+LAT1-4F2hc complex and its mutations were expressed and purified as previously described. The GFP-labeled protein was incubated with increasing concentrations of the native substrates (0.06nM to 2 μM) in 25 mM Hepes (pH 7.5), 150 mM NaCl, and 0.01% GDN buffer for 5 min on ice. The samples were loaded into standard MST capillaries, and measurements were performed at 25°C. The MST signal was detected at 800 nm with the laser power set to 40%. Data were analyzed using the MST optics. Affinity Analysis software (NanoTemper Technologies) was used to calculate the binding affinity via a one-site binding model. Control experiments using buffer alone and nonfluorescent ligand were conducted to assess nonspecific binding. All experiments were repeated in triplicate, and results are presented as the mean ± SD.

Whole-cell patch-clamp recordings

HEK-293T cells were cultured in Dulbecco's modified Eagle's medium (high glucose, Gibco) containing 10% fetal bovine serum (Gibco, USA) and streptomycin/penicillin (Thermo Fisher Scientific, USA). When the cells grew to 70% density, transfections of y^+LAT1 or its mutants together with 4F2hc were performed by using Lipofectamine 2000 (Thermo Fisher Scientific, USA) with 2.5 μg of DNA for each plasmid plus 0.5 μg of plasmid of GFP. Eight hours after transfection, the medium with DNA-lipid complex was removed and replaced by a fresh medium. Forty-eight hours after transfection, the cells were reseeded onto poly-D-lysine–coated coverslips 4 hours before the patch-clamp recordings. For the whole-cell recording, patch pipettes (3 to 7 megohm) that were fabricated from 1.0-mm capillary glass using a P-97 puller were used to record currents with an EPC-10 USB amplifier (HEKA). The bath solution contained 140 mM NaCl, 5 mM KCl, 2 mM $MgCl_2$, 2 mM $CaCl_2$, 10 mM glucose, and 10 mM Hepes, adjusted to pH 7.4 with NaOH. The bath solution without Na^+ contained 140 mM ChoCl, 5 mM KCl, 2 mM $MgCl_2$, 2 mM $CaCl_2$, 10 mM glucose, and 10 mM Hepes, adjusted to pH 7.4 with tris. The pipette solution contained 126 mM K-gluconate, 10 mM NaCl, 1 mM $MgCl_2$, 10 mM Hepes, and 10 mM EGTA, adjusted to pH 7.4 with KOH. The recording chamber (1500 μl) was continuously superfused at 2 ml/min.

Confocal imaging

Immunostaining was performed to check the expression level of y^+LAT1 and its mutants. The transfected cells were fixed in 4% paraformaldehyde for 30 min at room temperature. The cells were then washed three times with phosphate-buffered saline (PBS), blocked with 5% donkey serum with 0.1% Triton X-100 in PBS for 1 hour at room temperature, and then incubated overnight at 4°C with the primary antibody: anti-FLAG antibody (mouse, 1:1000; Sino Biological, 109143-MM13). The coverslips were washed in PBS and incubated with the secondary antibody (1:400; fluorescein isothiocyanate–donkey anti-mouse, Jackson ImmunoResearch, 715-165-150) for 1 hour at room temperature. The coverslips were then washed with PBS and mounted in Fluroshield with 4′,6-diamidino-2-phenylindole (Sigma-Aldrich, USA). GFP was fused to the N terminus of y^+LAT1 and its various mutants and then cotransfected them with 4F2hc in 293T cells to observe the membrane expression patterns. Images were obtained by a confocal laser scanning microscope LSM 980 (Zeiss, Germany). Each group has four coverslips, and two pictures were taken from each cover glass.

Western blot

Cells were transfected with y^+LAT1, and its mutants were lysed in radioimmunoprecipitation assay lysis buffer (Beyotime, China) with protease inhibitors (Roche, Germany) and phosphatase inhibitors (Roche, Germany). The homogenate was centrifuged at 12,000 rpm for 20 min, and the sediment was discarded. The concentration of protein was measured by an enhanced Bicinchoninic Acid Assay (BCA) protein assay kit (Beyotime, China). Samples were run on SurePAGETM (GenScipy, China) and then transferred to polyvinylidene difluoride membranes (Sigma-Aldrich, USA). Blots were incubated in 5% no-fat milk for 2 hours at room temperature for blocking and then probed and anti-FLAG (mouse, 1:1000; Sino Biological, 109143-MM13) overnight at 4°C. After washing, horseradish peroxidase (HRP)–conjugated anti-mouse antibody (goat, 1:1000; Abcam, ab205719) was incubated for 2 hours at room temperature. HRP-conjugated glyceraldehyde phosphate dehydrogenase (1:10,000; Proteintech, HRP-60004) was used as a loading control. Immunoblot analysis was performed with enhanced chemiluminescent immunoblot detection reagents (NCM Biotech, China) and analyzed with ImageJ.

Supplementary Materials

The PDF file includes:

Figs. S1 to S13
Table S1
Legend for movie S1

Other Supplementary Material for this manuscript includes the following:

Movie S1

REFERENCES AND NOTES

1. S. Bröer, M. Palacin, The role of amino acid transporters in inherited and acquired diseases. *Biochem. J.* **436**, 193–211 (2011).
2. P. M. Taylor, Role of amino acid transporters in amino acid sensing. *Am. J. Clin. Nutr.* **99**, 223S–230S (2014).
3. P. Kandasamy, G. Gyimesi, Y. Kanai, M. A. Hediger, Amino acid transporters revisited: New views in health and disease. *Trends Biochem. Sci.* **43**, 752–789 (2018).
4. D. Fotiadis, Y. Kanai, M. Palacin, The SLC3 and SLC7 families of amino acid transporters. *Mol. Aspects Med.* **34**, 139–158 (2013).
5. L. Mastroberardino, B. Spindler, R. Pfeiffer, P. J. Skelly, J. Loffing, C. B. Shoemaker, F. Verrey, Amino-acid transport by heterodimers of 4F2hc/CD98 and members of a permease family. *Nature* **395**, 288–291 (1998).
6. Y. Kanai, H. Segawa, K. Miyamoto, H. Uchino, E. Takeda, H. Endou, Expression cloning and characterization of a transporter for large neutral amino acids activated by the heavy chain of 4F2 antigen (CD98). *J. Biol. Chem.* **273**, 23629–23632 (1998).
7. R. G. Wells, W. S. Lee, Y. Kanai, J. M. Leiden, M. A. Hediger, The 4F2 antigen heavy chain induces uptake of neutral and dibasic amino acids in Xenopus oocytes. *J. Biol. Chem.* **267**, 15285–15288 (1992).

8. F. Verrey, E. I. Closs, C. A. Wagner, M. Palacin, H. Endou, Y. Kanai, CATs and HATs: The SLC7 family of amino acid transporters. *Pflugers Arch* **447**, 532–542 (2004).
9. R. Yan, X. Zhao, J. Lei, Q. Zhou, Structure of the human LAT1-4F2hc heteromeric amino acid transporter complex. *Nature* **568**, 127–130 (2019).
10. A. Rosell, M. Meury, E. Alvarez-Marimon, M. Costa, L. Perez-Cano, A. Zorzano, J. Fernandez-Recio, M. Palacin, D. Fotiadis, Structural bases for the interaction and stabilization of the human amino acid transporter LAT2 with its ancillary protein 4F2hc. *Proc. Natl. Acad. Sci. U.S.A.* **111**, 2966–2971 (2014).
11. R. H. Yan, J. Y. Zhou, Y. N. Li, J. L. Lei, Q. Zhou, Structural insight into the substrate recognition and transport mechanism of the human LAT2-4F2hc complex. *Cell Discov.* **6**, 82 (2020).
12. R. Yan, E. Xie, Y. Li, J. Li, Y. Zhang, X. Chi, X. Hu, L. Xu, T. Hou, B. R. Stockwell, J. Min, Q. Zhou, F. Wang, The structure of erastin-bound xCT-4F2hc complex reveals molecular mechanisms underlying erastin-induced ferroptosis. *Cell Res.* **32**, 687–690 (2022).
13. D. K. Kim, S. G. Ahn, J. C. Park, Y. Kanai, H. Endou, J. H. Yoon, Expression of L-type amino acid transporter 1 (LAT1) and 4F2 heavy chain (4F2hc) in oral squamous cell carcinoma and its precusor lesions. *Anticancer Res.* **24**, 1671–1675 (2004).
14. M. Toyoda, K. Kaira, Y. Ohshima, N. S. Ishioka, M. Shino, K. Sakakura, Y. Takayasu, K. Takahashi, H. Tominaga, N. Oriuchi, S. Nagamori, Y. Kanai, T. Oyama, K. Chikamatsu, Prognostic significance of amino-acid transporter expression (LAT1, ASCT2, and xCT) in surgically resected tongue cancer. *Br. J. Cancer* **110**, 2506–2513 (2014).
15. K. Kaira, N. Oriuchi, H. Imai, K. Shimizu, N. Yanagitani, N. Sunaga, T. Hisada, S. Tanaka, T. Ishizuka, Y. Kanai, H. Endou, T. Nakajima, M. Mori, L-type amino acid transporter 1 and CD98 expression in primary and metastatic sites of human neoplasms. *Cancer Sci.* **99**, 2380–2386 (2008).
16. L. Feliubadaló, M. Font, J. Purroy, F. Rousaud, X. Estivill, V. Nunes, E. Golomb, M. Centola, I. Aksentijevich, Y. Kreiss, B. Goldman, M. Pras, D. L. Kastner, E. Pras, P. Gasparini, L. Bisceglia, E. Beccia, M. Gallucci, L. de Sanctis, A. Ponzone, G. F. Rizzoni, L. Zelante, M. T. Bassi, A. L. George Jr., M. Manzoni, A. De Grandi, M. Riboni, J. K. Endsley, A. Ballabio, G. Borsani, N. Reig, E. Fernández, R. Estévez, M. Pineda, D. Torrents, M. Camps, J. Lloberas, A. Zorzano, M. Palacín, Non-type I cystinuria caused by mutations in *SLC7A9*, encoding a subunit ($b^{0,+}$AT) of rBAT. *Nat. Genet.* **23**, 52–57 (1999).
17. D. Torrents, R. Estevez, M. Pineda, E. Fernandez, J. Lloberas, Y. B. Shi, A. Zorzano, M. Palacin, Identification and characterization of a membrane protein (y^+L amino acid transporter-1) that associates with 4F2hc to encode the amino acid transport activity y^+L. A candidate gene for lysinuric protein intolerance. *J. Biol. Chem.* **273**, 32437–32445 (1998).
18. O. Yanagida, Y. Kanai, A. Chairoungdua, D. K. Kim, H. Segawa, T. Nii, S. H. Cha, H. Matsuo, J. Fukushima, Y. Fukasawa, Y. Tani, Y. Taketani, H. Uchino, J. Y. Kim, J. Inatomi, I. Okayasu, K. Miyamoto, E. Takeda, T. Goya, H. Endou, Human L-type amino acid transporter 1 (LAT1): Characterization of function and expression in tumor cell lines. *Biochim. Biophys. Acta* **1514**, 291–302 (2001).
19. A. Nabeyama, A. Kurita, K. Asano, Y. Miyake, T. Yasuda, I. Miura, G. Nishitai, S. Arakawa, S. Shimizu, S. Wakana, H. Yoshida, M. Tanaka, xCT deficiency accelerates chemically induced tumorigenesis. *Proc. Natl. Acad. Sci. U.S.A.* **107**, 6436–6441 (2010).
20. R. Pfeiffer, G. Rossier, B. Spindler, C. Meier, L. Kuhn, F. Verrey, Amino acid transport of y^+L-type by heterodimers of 4F2hc/CD98 and members of the glycoprotein-associated amino acid transporter family. *EMBO J.* **18**, 49–57 (1999).
21. D. Torrents, J. Mykkanen, M. Pineda, L. Feliubadalo, R. Estevez, R. de Cid, P. Sanjurjo, A. Zorzano, V. Nunes, K. Huoponen, A. Reinikainen, O. Simell, M. L. Savontaus, P. Aula, M. Palacin, Identification of *SLC7A7*, encoding y^+LAT-1, as the lysinuric protein intolerance gene. *Nat Genet* **21**, 293–296 (1999).
22. G. Borsani, M. T. Bassi, M. P. Sperandeo, A. De Grandi, A. Buoninconti, M. Riboni, M. Manzoni, B. Incerti, A. Pepe, G. Andria, A. Ballabio, G. Sebastio, *SLC7A7*, encoding a putative permease-related protein, is mutated in patients with lysinuric protein intolerance. *Nat Genet.* **21**, 297–301 (1999).
23. Y. Shoji, A. Noguchi, Y. Shoji, M. Matsumori, Y. Takasago, M. Takayanagi, Y. Yoshida, K. Ihara, T. Hara, S. Yamaguchi, M. Yoshino, M. Kaji, S. Yamamoto, A. Nakai, A. Koizumi, Y. Hokezu, K. Nagamatsu, H. Mikami, I. Kitajima, G. Takada, Five novel *SLC7A7* variants and y^+L gene-expression pattern in cultured lymphoblasts from Japanese patients with lysinuric protein intolerance. *Hum. Mutat.* **20**, 375–381 (2002).
24. H. de Ogier Baulny, M. Schiff, C. Dionisi-Vici, Lysinuric protein intolerance (LPI): A multi organ disease by far more complex than a classic urea cycle disorder. *Mol. Genet. Metab.* **106**, 12–17 (2012).
25. W. Mauhin, F. Habarou, S. Gobin, A. Servais, A. Brassier, C. Grisel, C. Roda, G. Pinto, D. Moshous, F. Ghalim, P. Krug, N. Deltour, C. Pontoizeau, S. Dubois, M. Assoun, L. Galmiche, J.-P. Bonnefont, C. Ottolenghi, J. de Blic, J.-B. Arnoux, P. de Lonlay, Update on lysinuric protein intolerance, a multi-faceted disease retrospective cohort analysis from birth to adulthood. *Orphanet J. Rare Dis.* **12**, 3 (2017).
26. Y. Lee, P. Wiriyasermkul, C. Jin, L. Quan, R. Ohgaki, S. Okuda, T. Kusakizako, T. Nishizawa, K. Oda, R. Ishitani, T. Yokoyama, T. Nakane, M. Shirouzu, H. Endou, S. Nagamori, Y. Kanai, O. Nureki, Cryo-EM structure of the human L-type amino acid transporter 1 in complex with glycoprotein CD98hc. *Nat. Struct. Mol. Biol.* **26**, 510–517 (2019).
27. R. Yan, Y. Li, J. M. Y. Zhang, S. Singer, L. Xia, X. Zhong, J. Gertsch, K.-H. Altmann, Q. Zhou, Mechanism of substrate transport and inhibition of the human LAT1-4F2hc amino acid transporter. *Cell Discov.* **7**, 16 (2021).
28. Z. Hu, R. Yan, Structural basis for the inhibition mechanism of LAT1-4F2hc complex by JPH203. *Cell Discov.* **10**, 73 (2024).
29. E. Errasti-Murugarren, J. Fort, P. Bartoccioni, L. Díaz, E. Pardon, X. Carpena, M. Espino-Guarch, A. Zorzano, C. Ziegler, J. Steyaert, J. Fernández-Recio, I. Fita, M. Palacín, L amino acid transporter structure and molecular bases for the asymmetry of substrate interaction. *Nat. Commun.* **10**, 1807 (2019).
30. Y. Fang, H. Jayaram, T. Shane, L. Kolmakova-Partensky, F. Wu, C. Williams, Y. Xiong, C. Miller, Structure of a prokaryotic virtual proton pump at 3.2 A resolution. *Nature* **460**, 1040–1043 (2009).
31. X. Gao, F. Lu, L. Zhou, S. Dang, L. Sun, X. Li, J. Wang, Y. Shi, Structure and mechanism of an amino acid antiporter. *Science* **324**, 1565–1568 (2009).
32. X. Gao, L. Zhou, X. Jiao, F. Lu, C. Yan, X. Zeng, J. Wang, Y. Shi, Mechanism of substrate recognition and transport by an amino acid antiporter. *Nature* **463**, 828–832 (2010).
33. K. E. J. Jungnickel, J. L. Parker, S. Newstead, Structural basis for amino acid transport by the CAT family of SLC7 transporters. *Nat. Commun.* **9**, 550 (2018).
34. M. Meury, M. Costa, D. Harder, M. Stauffer, J. M. Jeckelmann, B. Bruhlmann, A. Rosell, H. Ilgu, K. Kovar, M. Palacin, D. Fotiadis, Detergent-induced stabilization and improved 3D map of the human heteromeric amino acid transporter 4F2hc-LAT2. *PLOS ONE* **9**, e109882 (2014).
35. J.-M. Jeckelmann, D. Fotiadis, Volta phase plate cryo-EM structure of the human heterodimeric amino acid transporter 4F2hc-LAT2. *Int. J. Mol. Sci.* **20**, 931 (2019).
36. C. F. Rodriguez, P. Escudero-Bravo, L. Díaz, P. Bartoccioni, C. García-Martín, J. G. Gilabert, J. Boskovic, V. Guallar, E. Errasti-Murugarren, O. Llorca, M. Palacin, Structural basis for substrate specificity of heteromeric transporters of neutral amino acids. *Proc. Natl. Acad. Sci. U. S. A.* **118**, e2113573118 (2021).
37. J. L. Parker, J. C. Deme, D. Kolokouris, G. Kuteyi, P. C. Biggin, S. M. Lea, S. Newstead, Molecular basis for redox control by the human cystine/glutamate antiporter system xc. *Nat. Commun.* **12**, 7147 (2021).
38. J. Rullo-Tubau, M. Martinez-Molledo, P. Bartoccioni, I. Puch-Giner, Á. Arias, S. Saen-Oon, C. Stephan-Otto Attolini, R. Artuch, L. Díaz, V. Guallar, E. Errasti-Murugarren, M. Palacín, O. Llorca, Structure and mechanisms of transport of human Asc1/CD98hc amino acid transporter. *Nat. Commun.* **15**, 2986 (2024).
39. Y. Li, Y. Guo, A. Bröer, L. Dai, S. Bröer, R. Yan, Cryo-EM structure of the human Asc-1 transporter complex. *Nat. Commun.* **15**, 3036 (2024).
40. G. Lamoureux, E. A. Orabi, Molecular modelling of cation–π interactions. *Mol. Simulat.* **38**, 704–722 (2012).
41. M. P. Sperandeo, P. Annunziata, V. Ammendola, V. Fiorito, A. Pepe, M. V. Soldovieri, M. Taglialatela, G. Andria, G. Sebastio, Lysinuric protein intolerance: Identification and functional analysis of mutations of the SLC7A7 gene. *Hum. Mutat.* **25**, 410 (2005).
42. C. Gopalakrishnan, A. M. Al-Subaie, N. N, H. Y. Yeh, I. A. Tayubi, B. Kamaraj, Prioritization of SNPs in y+LAT-1 culpable of lysinuric protein intolerance and their mutational impacts using protein-protein docking and molecular dynamics simulation studies. *J. Cell. Biochem.* **120**, 18496–18508 (2019).
43. R. Yan, Y. Li, Y. Shi, J. Zhou, J. Lei, J. Huang, Q. Zhou, Cryo-EM structure of the human heteromeric amino acid transporter $b^{0,+}$ AT-rBAT. *Sci. Adv.* **6**, eaay6379 (2020).
44. S. Bröer, N. Brookes, Transfer of glutamine between astrocytes and neurons. *J. Neurochem.* **77**, 705–719 (2001).
45. K. Kazmier, D. P. Claxton, H. S. McHaourab, Alternating access mechanisms of LeuT-fold transporters: Trailblazing towards the promised energy landscapes. *Curr. Opin. Struct. Biol.* **45**, 100–108 (2017).
46. D. Ma, P. Lu, C. Yan, C. Fan, P. Yin, J. Wang, Y. Shi, Structure and mechanism of a glutamate-GABA antiporter. *Nature* **483**, 632–636 (2012).
47. X. Chi, X. Li, Y. Chen, Y. Zhang, Q. Su, Q. Zhou, Cryo-EM structures of the full-length human KCC2 and KCC3 cation-chloride cotransporters. *Cell Res.* **31**, 482–484 (2021).
48. J. Lei, J. Frank, Automated acquisition of cryo-electron micrographs for single particle reconstruction on an FEI Tecnai electron microscope. *J. Struct. Biol.* **150**, 69–80 (2005).
49. S. Q. Zheng, E. Palovcak, J.-P. Armache, K. A. Verba, Y. Cheng, D. A. Agard, MotionCor2: Anisotropic correction of beam-induced motion for improved cryo-electron microscopy. *Nat. Methods* **14**, 331–332 (2017).
50. T. Grant, N. Grigorieff, Measuring the optimal exposure for single particle cryo-EM using a 2.6 Å reconstruction of rotavirus VP6. *eLife* **4**, e06980 (2015).
51. K. Zhang, Gctf: Real-time CTF determination and correction. *J. Struct. Biol.* **193**, 1–12 (2016).
52. D. Kimanius, B. O. Forsberg, S. H. Scheres, E. Lindahl, Accelerated cryo-EM structure determination with parallelisation using GPUs in RELION-2. *eLife* **5**, e18722 (2016).
53. S. H. Scheres, A Bayesian view on cryo-EM structure determination. *J. Mol. Biol.* **415**, 406–418 (2012).
54. S. H. Scheres, RELION: Implementation of a Bayesian approach to cryo-EM structure determination. *J. Struct. Biol.* **180**, 519–530 (2012).

55. S. H. Scheres, Semi-automated selection of cryo-EM particles in RELION-1.3. *J. Struct. Biol.* **189**, 114–122 (2015).
56. P. B. Rosenthal, R. Henderson, Optimal determination of particle orientation, absolute hand, and contrast loss in single-particle electron cryomicroscopy. *J. Mol. Biol.* **333**, 721–745 (2003).
57. S. Chen, G. McMullan, A. R. Faruqi, G. N. Murshudov, J. M. Short, S. H. Scheres, R. Henderson, High-resolution noise substitution to measure overfitting and validate resolution in 3D structure determination by single particle electron cryomicroscopy. *Ultramicroscopy* **135**, 24–35 (2013).
58. A. Punjani, J. L. Rubinstein, D. J. Fleet, M. A. Brubaker, cryoSPARC: Algorithms for rapid unsupervised cryo-EM structure determination. *Nat. Methods* **14**, 290–296 (2017).
59. P. D. Adams, P. V. Afonine, G. Bunkoczi, V. B. Chen, I. W. Davis, N. Echols, J. J. Headd, L. W. Hung, G. J. Kapral, R. W. Grosse-Kunstleve, A. J. McCoy, N. W. Moriarty, R. Oeffner, R. J. Read, D. C. Richardson, J. S. Richardson, T. C. Terwilliger, P. H. Zwart, PHENIX: A comprehensive Python-based system for macromolecular structure solution. *Acta Crystallogr. D Biol. Crystallogr.* **66**, 213–221 (2010).
60. P. Emsley, B. Lohkamp, W. G. Scott, K. Cowtan, Features and development of Coot. *Acta Crystallogr. D Biol. Crystallogr.* **66**, 486–501 (2010).
61. L. G. Trabuco, E. Villa, K. Mitra, J. Frank, K. Schulten, Flexible fitting of atomic structures into electron microscopy maps using molecular dynamics. *Structure* **16**, 673–683 (2008).

Acknowledgments: We thank the Cryo-EM Facility of Southern University of Science and Technology (SUSTech) and the Cryo-EM Facility and the High-Performance Computing Center of Westlake University for providing the facility support. We thank S. Xu, L. Zhang, Y. Gao, and P. Li at the Cryo-EM Center of SUSTech for technical support in electron microscopy data acquisition. We thank Z. Liu for technical support on computing environment. R.Y. is an investigator of SUSTech Institute for Biological Electron Microscopy. **Funding:** This work was funded by the National Natural Science Foundation of China (32371267 to R.Y. and 82101297 to Z.W.), the National Key R&D Program of China (2020YFA0509300 to Q.Zh.) from Ministry of Science and Technology of China, the Major Talent Recruitment Program of Guangdong Province (2021QNO2Y167 to R.Y. and 2021QN020751 to Z.W.), the Scientific Research and Innovation Project of Medical Discipline (G030410001 to R.Y.), and the Shenzhen Medical Research Fund (A2303046 to R.Y. and C2301006 to Z.W.). **Author contributions:** R.Y., Z.W., and Q.Zh. conceived the project and designed the experiments. L.D. and Y.L. did the molecular cloning, protein purification, cryo-EM data collection, and processing. T.Z. and Y.Z. did the model building and analysis. Q.Z. did the cell-based transport assays. Y.S. did the MD simulations assay. K.X. did the immunostaining and Western blot. All the authors contributed to the data analysis. R.Y., Q.Zh., Z.W., and J.H. wrote the manuscript. **Competing interests:** The authors declare that they have no competing interests. **Data and materials availability:** Cryo-EM maps and molecular models have been securely archived in the EM Data Bank and PDB, respectively. Specifically, the following structures have been deposited in the PDB (http://rcsb.org) and the Electron Microscopy Data Bank (https://ebi.ac.uk/pdbe/emdb): apo (PDB 9KH5, complete map EMD-62332), the complex of y^+LAT1-4F2hc bound with Arg (PDB 8YLP, complete map EMD-39388), the locally refined structure of the y^+LAT1-4F2hc bound with Arg (PDB 9KJU, locally refined map EMD-62377), the structure of y^+LAT1 bound with Lys (PDB 8XYJ, complete map EMD-38775), and y^+LAT1 bound with Leu (PDB 8XXI, complete map EMD-38750). All data needed to evaluate the conclusions in the paper are present in the paper and/or the Supplementary Materials. The cDNA of y^+LAT1 and 4F2hc in the pCAG vector can be provided by Q.Zh. (Westlake University) pending scientific review and a completed material transfer agreement. Requests for the related plasmids should be submitted to Q.Zh. (Westlake University).

Submitted 24 April 2024
Accepted 12 February 2025
Published 19 March 2025
10.1126/sciadv.adq0558